Marine Ice Cliff Instability Mitigated by Slow Removal of Ice Shelves

Fiona Clerc[1], Brent M. Minchew[2], and Mark D. Behn[3]

[1]MIT-WHOI Joint Program in Oceanography/Applied Ocean Science & Engineering, Cambridge MA

[2]Department of Earth, Atmospheric and Planetary Sciences, Massachusetts Institute of Technology, Cambridge MA

[3]Department of Earth and Environmental Sciences, Boston College, Chestnut Hill MA

Corresponding author: Fiona Clerc (fclerc@mit.edu)

Key Points:

- The critical height required for the collapse of marine ice cliffs increases with the timescale of buttressing ice-shelf removal.
- Over short timescales, deformation is primarily elastic; a 90-m cliff (a previous threshold) may fail if removal occurs in under an hour.
- Over timescales longer than days (as in the Larsen B collapse), deformation is by viscous, ductile flow for cliffs shorter than ~540 m.

Abstract

The accelerated calving of ice shelves buttressing the Antarctic Ice Sheet may form unstable ice cliffs. The marine ice-cliff instability (MICI) hypothesis posits that cliffs taller than a critical height (~90-m) will undergo structural collapse, initiating runaway retreat in ice-sheet models. This critical height is based on inferences from pre-existing, static ice cliffs. Here we show how critical height increases with the timescale of ice-shelf collapse. We model failure mechanisms within an ice cliff deforming after removal of ice-shelf buttressing stresses. If removal occurs rapidly, the cliff deforms primarily elastically and fails through tensile-brittle fracture, even at relatively small cliff heights. As the ice-shelf removal timescale increases, viscous relaxation dominates, and the critical height increases to ~540 m for timescales > days. A 90-m critical height implies ice-shelf removal in under an hour. Incorporation of ice-shelf collapse timescales in prognostic ice-sheet models will mitigate MICI, implying less ice-mass loss.

Plain Language Summary

The seaward flow of ice from grounded ice sheets to the ocean is often resisted by the buttressing effect of floating ice shelves. These ice shelves risk collapsing as the climate warms, potentially exposing tall cliff faces. Some suggest ice cliffs taller than ~90 m could collapse under their own weight, exposing taller cliffs further to the interior of a thickening ice sheet, leading to runaway ice-sheet retreat. This model, however, is based on studies of pre-existing cliffs found at calving fronts. In this study, we consider the transient case, examining the processes by which an ice cliff forms as a buttressing ice shelf is removed. We show that the height at which a cliff collapses increases with the timescale of ice-shelf removal. If the ice shelf is removed rapidly, deformation may be concentrated, forming vertical cracks and potentially leading to the collapse of small (e.g., 90-m) cliffs. However, if we consider ice-shelf collapse timescales longer than a few days

(consistent with observations), deformation is distributed throughout the cliff, which flows viscously rather than collapsing. We expect including the effects of such ice-shelf collapse timescales in future ice-sheet models would mitigate runaway cliff collapse and reduce predicted ice-sheet mass loss.

1. Introduction

Floating ice shelves impart resistive stresses on the seaward margins of grounded ice sheets, playing an important role in their stabilization. Buttressing ice shelves are vulnerable to calving and collapse under warming climates, driving uncertainty in magnitudes and rates of future sea-level rise. The 2002 collapse of the Larsen B Ice Shelf is a dramatic example of ice-shelf vulnerability. Larsen B, on the eastern Antarctic Peninsula, likely existed throughout the Holocene (Domack et al., 2005) before shattering into icebergs within 1–3 weeks (Rack & Rott, 2004). Sergienko & Macayeal (2005) attributed this collapse to enhanced surface melting. Subsequent accelerated fluxes from glaciers feeding Larsen B illustrate the potential impact of climate warming on ice-sheet loss (Rignot et al., 2004; Scambos et al., 2004).

While the acceleration of glacier flow following the loss of a buttressing ice shelf is well-studied (Haseloff & Sergienko, 2018; Pegler, 2018b, 2018a; Schoof, 2007), the dynamic response of an ice sheet to sudden changes in ice-shelf buttressing stress is not fully understood. Some predict a warming climate will increase meltwater-driven hydrofracturing, leading to ice shelf breakup and the formation of ice cliffs prone to structural collapse above a critical height (DeConto & Pollard, 2016; Pollard et al., 2015). If the newly unbuttressed ice sheet thickens inland, cliff failure will lead to the progressive exposure of taller cliffs, initiating the runaway collapse of the ice sheet in a process sometimes called the marine ice-cliff instability (MICI). To date, implementation of MICI in ice-sheet models has been based on critical cliff heights of ~90 m, parameterized from studies of pre-existing, static ice cliffs found at calving fronts (e.g., Bassis & Walker, 2012; Parizek et al., 2019). However, it remains unclear whether the same physics govern ice cliffs formed as an ice shelf is removed over a finite timescale. Specifically, the deformation mechanisms that accommodate stress in the ice (i.e., brittle versus ductile) are sensitive to the ice-shelf removal timescale. Over longer timescales, ice tends to deform ductilely, resulting in deformation that is distributed throughout a cliff instead of localized along a fracture. Additionally, ice prone to MICI (in the Antarctic interior) is mostly intact and more likely to undergo ductile deformation than damaged ice at calving fronts undergoing brittle fracture. Ductile deformation, absent brittle fracture, would mitigate MICI.

Here we use a 1-D analytical and 2-D numerical viscoelastic model to examine the response of idealized cliffs to the removal of backstresses over various timescales and subaerial cliff heights. We use the stresses and strain rates from our models to delineate the modes of deformation within an ice cliff based on constraints from laboratory experiments. We predict whether fractures form or large-scale viscous flow mitigates MICI.

2. Methods

2.1 Deformation mechanisms in an ice cliff

At moderately low strain rates, deformation in ice is accommodated by dislocation creep (Goldsby & Kohlstedt, 2001) and may be characterized by a non-Newtonian (shear-thinning) viscous flow law (Glen, 1955). At higher strain rates, existing microcracks may grow, interlink, and form large-scale faults. Macroscopic failure is observed above a critical strain rate, which depends on the deformation regime (**Figure 1a**). The mode of failure is controlled by the coefficient of internal friction (μ) of ice and the confinement, expressed as a ratio, R, of the least- to most-compressive stresses (Golding et al., 2012; Renshaw & Schulson, 2001). Under low confinement or extension (R<0.01), ice is in a "Tensile" deformation regime. Above a tensile brittle-ductile strain rate of 4×10^{-7} 1/s (dashed red line, **Figure 1a**), vertical cracks interlink to form vertical faults (Schulson & Duval, 2009). Under low to moderate confinement (0.01<R<(1-μ)/(1+μ)) ice deforms in the "Coulombic" deformation regime. In this regime, compression induces slip along frictional shear cracks, which form tensile "wing" cracks at their edges. At strain rates above a critical compressive brittle-ductile strain rate (~10^{-5} 1/s, solid red line, **Figure 1a**), these wing cracks may interlink to form a macroscopic "Coulombic" fault. Finally, under high confinement (R>(1-μ)/(1+μ)), ice deforms in the "Thermal Softening" regime. In this regime, high strain rates (~1.2×10^{-2} 1/s; dotted red line, **Figure 1a**) and high strains can result in localized adiabatic heating, leading to thermal softening and the formation of a "plastic" shear fault (Golding et al., 2012; Schulson, 2002). We hereafter reserve the term "plastic" to describe macroscopic rheological behavior, such that it describes failure under all modes discussed here.

Previous studies parametrized ice cliff failure using the Mohr-Coulomb criterion, presuming Coulombic failure accompanied by tensile cracks (Bassis & Walker, 2012; DeConto & Pollard, 2016). However, this failure mode represents only a sub-space of possible deformation modes (**Figure 1a**). By evaluating the strain rates and confinement ratios within an ice cliff, we can assess which deformation mechanisms are present, and whether failure likely occurs.

2.2 Model set-up

To evaluate the mode of deformation within an ice cliff, we consider a rectangular block of ice of total thickness H (**Figure 1b**). Initially, the cliff is supported by a mirrored block of ice, representing the buttressing ice shelf. The cliff is in glaciostatic equilibrium as deviatoric and shear stresses are zero. Over a finite transition time Δt, the supporting ice shelf is thinned at a linear rate exposing an unsupported subaerial cliff of height h and a partially supported submarine cliff of height D (**Figure 1c**). Here, D is the water depth and the base of the domain is the glacier bed/seafloor. We assume a free-slip basal boundary condition; we investigate the effects of a no-slip boundary condition as in Ma et al. (2017), in section S2.5 of the supplement. The edge of the cliff is at the grounding line, thus the cliff is at flotation ($\rho_i H=\rho_w D$).

We assume a Maxwell viscoelastic rheology to relate the deviatoric stress (τ_{ij}) and strain-rate ($\dot{\epsilon}_{ij}$) tensors in the ice cliff (see section S1.2; Gudmundsson, 2011). Tensile stresses are positive, and depth (y) is positive downward. The Maxwell relation is characterized by a relaxation time $t_R=\eta_{eff}/G$ (η_{eff} is the effective dynamic viscosity and G is the shear modulus) describing the timescale over which stresses relax in response to an applied strain. The other timescale relevant to this study is the transition time (Δt) over which ice-shelf buttressing stresses are removed. For transition times longer than the relaxation time ($\Delta t>t_R$), the ice cliff deforms primarily by viscous creep; for shorter transition times the cliff deforms elastically. Extended methods describing our 1-D analytic and 2-D numerical approach for solving the evolution of stress and deformation modes within an ice cliff are found in sections S1 and S2.1.

3. Results

3.1 Analytical results

We first consider the case of a static ice cliff as represented by the final cliff geometry after the buttressing ice shelf is removed (**Figure 1c**). This geometry is equivalent to that considered by Bassis and Walker (2012), who calculated the average stresses acting on an entire ice cliff, to determine whether an ice wedge would detach along a Coulombic shear fault. However, rather than using the average stresses, we consider the local stresses, confinement ratios, and strain rates along the cliff face to predict the local mode of deformation and assess if and where fractures will initiate (see section S2.1). A similar analysis was performed on static cliffs at calving fronts by Parizek et al. (2019). Our analysis extends this work by considering the effects of elasticity, the Thermal Softening regime, material properties appropriate for undamaged ice, and the effects of buttressing stress removal and associated time dependence.

The mode of deformation and confinement ratio depends on the local depth within the ice cliff. Specifically, the most-compressive stress (σ_1) acting on the cliff face is the vertical overburden pressure (σ_{yy}), its magnitude increases linearly with depth (black line, **Figure 2a**). The horizontal least-compressive stress (σ_{xx}=σ_3) acting on the cliff face is zero in the subaerial part of the cliff, but the stress magnitude increases linearly with depth after reaching sea-level due to the hydrostatic pressure of the water (green line, **Figure 2a**). Thus, the confinement ratio (R) is zero within the subaerial portion of the ice cliff, and then increases with depth below sea-level (**Figure 2b**). Locally, we expect the mode of deformation to be Tensile at subaerial depths (where R=0), transition to the Coulombic regime at moderate depths and confinement ratios (0.01>R>0.33), and transition to the Thermal Softening regime at greater depths (at R>0.33). As ice is weakest under lower confinement, the critical strain rate at which deformation becomes localized and forms large-scale faults (red lines in **Figure 1a**) increases with depth along the cliff face.

To assess whether deformation will be accommodated by viscous creep or localized plastic failure, we consider the time-dependent response of the cliff to the removal of a buttressing ice shelf over the transition time Δt. To do so, we calculate strain rates along the cliff face from the stress field, assuming a Maxwell viscoelastic rheology for ice (see sections S1.2 and S2.1). Strain rates are the sum of a viscous component (proportional to the stress) and an elastic component (proportional to the rate of stress change). We approximate the rate of stress change as the stress after ice-shelf removal divided by the transition time (Δt), as initially the cliff is fully buttressed and the deviatoric stress is zero. Thus, decreasing the removal time increases the elastic (and total) strain rate. We calculate effective deviatoric stresses (τ_e) and effective strain ratees ($\dot{\epsilon}_e$), defined as the square root of the second invariant of the deviatoric stress and strain-rate tensors, respectively. The cliff face is free of shear stresses, such that the effective stresses and strain rates depend on the deviatoric stress only. In our simplified 1-D geometry of the cliff face, the local effective stress is the magnitude of the deviatoric stress ($\tau_e=\sqrt{(\tau_{kl}\tau_{lk}/2)}=(\sigma_1-\sigma_3)/2$). The effective stress initially increases with depth due to the overburden ice pressure, and then decreases with depth once sea-level is reached due to the water pressure (orange/magenta/cyan lines, **Figure 2a**). The local effective strain rate scales with the effective stress and is also greatest at sea-level (y=h).

We predict if and where failure will occur within a cliff by considering calculated strain rates and confinement ratios within the deformation-regime framework (**Figure 1a**; section S2.1). For a 100-m cliff forming over 0.6 days (approximately the relaxation time, t_R=0.5 days for h=100 m), strain rates remain low (**Figure 2c,d**), implying deformation is accommodated by microscopic creep and that the cliff flows ductilely instead of collapsing. If we decrease the transition time below the relaxation time (e.g., $\Delta t=6 \times 10^{-4}$ days, magenta lines in **Figure 2c,d**), strain rates increase, locally reaching the tensile brittle-ductile transition near sea-level and thus entering the Tensile regime. If we instead increase the cliff height to 600 m, keeping Δt=0.6 days (longer than the relaxation time, t_R=0.01 days for h=600 m), the elastic response becomes negligible. However, the effective stress increases, raising strain rates into the Tensile regime (dashed cyan lines, **Figure 2**). Thus, we predict an ice cliff deforms ductilely, unless it is tall or the buttressing ice shelf is removed rapidly relative to the relaxation time. Further, because the difference between the local strain rate and the tensile brittle-ductile strain rate is greatest near sea-level, we expect failure initiates as near-vertical tensile fractures in this location (**Figure 2d**). Failure does not initiate in the Coulombic or Thermal Softening regimes.

Our analysis shows that the use of a Mohr-Coulomb yield-stress criterion alone may be an oversimplification because an ice cliff can undergo multiple modes of deformation at different confinement ratios (**Figure 2b**), corresponding to different depths within the cliff (**Figure 1a**). The validity of the Mohr-Coulomb failure criterion only holds for cliffs deforming under the Coulombic regime and characterized by low confinement ratios ($0<R<0.33$). At flotation (potentially the most relevant condition) the majority of the ice cliff will have a high average confinement ratio, implying it is deforming ductilely within the Thermal Softening regime. Because this regime can accommodate large strain rates through dislocation creep before failing via localized plastic faulting, macroscopic cliff deformation may be dominated by viscous flow.

3.2 Numerical results

The 1-D analytical model for strain rate along the face of an ice cliff as described above is useful; however, it does not capture the 2-D variability in stress and strain rate throughout an ice cliff, which could potentially promote failure at other locations within the cliff. This motivates our numerical analysis (described in detail within section S2.2 of the supplement), in which we explore the effects of non-Newtonian viscoelastic rheologies on ice-cliff deformation in the 2-D geometry shown in **Figure 1**. We use the model SiStER (Simple Stokes solver for Exotic Rheologies; Olive et al. (2016)) to run simulations over a range of subaerial cliff heights (h) and transition times (Δt) and evaluate the stress and strain-rate fields to determine if and where the cliff reaches our failure criteria.

In all cases, we find strain rates are highest near sea-level at the end of the transition (**Figure 3**; top row). From the stress field, we map the location of the deformation regimes within the cliff (**Figure 3**; middle row) and subtract the critical strain rate from the local strain rate to determine where and how the cliff fails (**Figure 3**; bottom row). The numerical model predicts that either the entire cliff undergoes ductile deformation (**Figure 3**; left column) or shallow portions of the cliff undergo failure in the Tensile regime (**Figure 3**; center/middle columns). Tensile brittle fractures initiate due to either rapid buttressing stress removal or large cliff heights. There is no scenario in which failure initiates in the Coulombic or Thermal Softening regimes, although such failure modes may follow the onset of tensile-brittle fracture. This is consistent with the deformation mode predictions made by the analytical model, over a range of cliff heights and transition times.

4. Implications for the marine ice cliff instability

Given the consistency between the results of the analytic and numerical models (see section S2.3), we extend the analytic model to conditions in nature and examine the implications of our cliff failure predictions for runaway cliff collapse. Specifically, we compare the tensile brittle-ductile strain rate to the analytically-derived local strain rate at sea-level and parametrize the initiation of Tensile failure according to cliff height and transition time (**Figure 4**). The local strain rates increase quickly within the elastic limit ($\Delta t<t_R$; black line, **Figure 4a**). Under these rapid transition times, tensile cracks are predicted even in small cliffs. However, for transition times longer than the Maxwell time, the elastic term vanishes, and the solution reaches a steady-state viscous limit. Even if we allow Glen's flow-law parameter ($A=\dot{\epsilon}_e/\tau_e^3$) to vary by an order of magnitude (green dash-dotted line, **Figure 4b**), we find strain rates are independent of the ice-shelf removal timescale for Δt>~1 day. In this viscous limit, the critical subaerial height remains constant at ~540 m, independent of the timescale and flow-law parameter. Assuming the total ice thickness is constant at H=1 km (instead of keeping the cliff at flotation) increases the effective viscosity and decreases the critical height to ~400 m for longer transition times (gray line, **Figure 4b**). Finally, our model assumes the ice is initially static whereas ice near the grounding line may have softened due to shear-thinning. We may thus be overestimating effective viscosities and overpredicting brittle failure, at timescales of 10^{-4}–10^{-1} days (compare dashed and solid green line, **Figure 4b**).

We examine the dependence of our solution on the assumed material properties of ice. Changing the grain size (which sets the crack length in intact ice) and fracture toughness within the range of experimental observations changes the tensile brittle-ductile strain rate (Lee & Schulson, 1988; Schulson & Duval, 2009), and thus the critical subaerial height. The 540-m critical height (in the viscous limit) corresponds to a grain size of ~1 mm and a fracture toughness of 100 kPa $m^{1/2}$ for our assumed flow-law parameter ($A=1.2\times10^{-25}$ s^{-1} Pa^{-3}; Cuffey & Paterson, (2010)). If we include the range of plausible grain size of 1–8 mm (Gow et al., 1997) and of fracture toughness of 80–120 kPa $m^{1/2}$ (Schulson & Duval, 2009), the critical height in the viscous limit ranges from 170–710 m (green zone, **Figure 4b**). By contrast, prescribing a fracture toughness of 50 kPa $m^{1/2}$ and crack half-length of 50 mm (values chosen for damaged ice at calving fronts by Parizek et al. (2019)) yields a 60-m critical height (see **Figure S4** for critical height versus fracture toughness/crack half-length). Our prediction that a cliff formed at the grounding line could be stable at great (~540-m) heights assumes the ice is undamaged. However, even in damaged ice, the rapid retreat of grounding lines would quickly reach undamaged ice within the interior of the ice sheet, potentially stabilizing further retreat. In addition, we caution that the propagation of tensile cracks would influence the strain-rate and stress fields and may affect subsequent failure (e.g., Coulombic or shear faulting considered by Parizek et al. (2019) and Bassis and Walker (2012), respectively).

In summary, we predict the critical cliff height necessary for failure increases with the timescale of ice-shelf buttressing stress removal. In their parametrization of cliff failure within an Antarctic ice sheet model, DeConto and Pollard (2016) prescribe a critical height of 90 m. In our model, the formation of tensile cracks within a 90-m cliff requires an elastic response and implies the removal of buttressing ice shelves over timescales less than an hour (see intersection of yellow/green lines in **Figure 4a**). To determine whether such timescales are realistic, we compare them with the duration of the Larsen B Ice Shelf collapse. Satellite images show Larsen B disintegrated over at least a week (Rack & Rott, 2004). A recent model of ice-shelf collapse by hydrofracture of melt ponds (Robel & Banwell, 2019) proposed that the rate of ice-shelf collapse is limited by localized interactions between melt ponds, and that Larsen B was a special case of exceptionally rapid collapse due to an anomalous melt season. As such, the removal of a buttressing ice shelf prior to the potential initiation of runaway cliff failure may take days to weeks (longer than the relaxation time of ice), implying the elastic limit of our solution is not physically relevant. The response is instead primarily viscous, and we predict cliff failure only initiates in cliffs taller than ~540 m. Below this critical height, the formation of tensile cracks is suppressed, and the cliff will flow viscously. As ice shelves likely detach over longer timescales, 90-m cliffs made of relatively intact ice would likely flow ductilely, mitigating runaway cliff failure.

Our results complement the recent finding by Edwards et al. (2019) that ice-cliff failure is not necessary to explain paleo sea-levels. We conclude that a model for cliff failure must account for the timing of ice-shelf collapse. This need is especially pronounced given the uncertainties associated with the critical cliff height calculations, and the effects of stress accommodation through ductile deformation. We expect incorporating longer ice-shelf collapse timescales in ice sheet models will decrease ice-sheet mass loss by cliff failure.

Acknowledgements: We thank Greg Hirth, Brad Hager, and Bill Durham for their useful comments. The manuscript benefited from constructive reviews by Dan Martin and an anonymous reviewer, and editorial handling by Mathieu Morlighem. This work was supported by an NSF-GRFP (Fiona Clerc), and NSF awards OPP-1739031 (Brent Minchew) and EAR-19-03897 (Mark Behn). Code reproducing our results is found at https://doi.org/10.5281/zenodo.3379074

References

Bassis, J. N., & Walker, C. C. (2012). Upper and lower limits on the stability of calving glaciers from the yield strength envelope of ice. In *Proceedings of the Royal Society A: Mathematical, Physical and Engineering Sciences*. https://doi.org/10.1098/rspa.2011.0422

Cuffey, K., & Paterson, W. (2010). *The physics of glaciers, 4th Edition*. *Elsevier* (Vol. 1).

https://doi.org/10.1016/0016-7185(71)90086-8

DeConto, R. M., & Pollard, D. (2016). Contribution of Antarctica to past and future sea-level rise. *Nature*, *531*(7596), 591–597. https://doi.org/10.1038/nature17145

Domack, E., Duran, D., Leventer, A., Ishman, S., Doane, S., McCallum, S., et al. (2005). Stability of the Larsen B ice shelf on the Antarctic Peninsula during the Holocene epoch. *Nature*, *436*(7051), 681–685. https://doi.org/10.1038/nature03908

Edwards, T. L., Brandon, M. A., Durand, G., Edwards, N. R., Golledge, N. R., Holden, P. B., et al. (2019). Revisiting Antarctic ice loss due to marine ice-cliff instability. *Nature*, *566*(7742), 58–64. https://doi.org/10.1038/s41586-019-0901-4

Glen, J. W. (1955). The creep of polycrystalline ice. *Proceedings of the Royal Society of London. Series A. Mathematical and Physical Sciences*, *228*(1175), 519--538.

Golding, N., Schulson, E. M., & Renshaw, C. E. (2012). Shear localization in ice: Mechanical response and microstructural evolution of P-faulting. *Acta Materialia*, *60*(8), 3616–3631. https://doi.org/10.1016/j.actamat.2012.02.051

Goldsby, D. L., & Kohlstedt, D. L. (2001). Superplastic deformation of ice: Experimental observations. *Journal of Geophysical Research: Solid Earth*. https://doi.org/10.1029/2000jb900336

Gow, A. J., Meese, D. A., Alley, R. B., Fitzpatrick, J. J., Anandakrishnan, S., Woods, G. A., & Elder, B. C. (1997). Physical and structural properties of the Greenland Ice Sheet Project 2 ice core: A review. *Journal of Geophysical Research: Oceans*. https://doi.org/10.1029/97JC00165

Gudmundsson, G. H. (2011). Ice-stream response to ocean tides and the form of the basal sliding law. *Cryosphere*, *5*(1), 259–270. https://doi.org/10.5194/tc-5-259-2011

Haseloff, M., & Sergienko, O. V. (2018). The effect of buttressing on grounding line dynamics. *Journal of Glaciology*. https://doi.org/10.1017/jog.2018.30

Lee, R. W., & Schulson, E. M. (1988). The Strength and Ductility of Ice Under Tension. *Journal of Offshore Mechanics and Arctic Engineering*, *110*(2), 187–191.

Ma, Y., Tripathy, C. S., & Bassis, J. N. (2017). Bounds on the calving cliff height of marine terminating glaciers. *Geophysical Research Letters*, *44*(3), 1369–1375. https://doi.org/10.1002/2016GL071560

Olive, J. A., Behn, M. D., Mittelstaedt, E., Ito, G., & Klein, B. Z. (2016). The role of elasticity in simulating long-term tectonic extension. *Geophysical Journal International*, *205*(2), 728–743. https://doi.org/10.1093/gji/ggw044

Parizek, B. R., Christianson, K., Alley, R. B., Voytenko, D., Vaňková, I., Dixon, T. H., et al. (2019). Ice-cliff failure via retrogressive slumping. *Geology*, *47*(5), 449–452. https://doi.org/10.1130/G45880.1

Pegler, S. S. (2018a). Marine ice sheet dynamics: the impacts of ice-shelf buttressing. *Journal of Fluid Mechanics*, *857*, 605–647. https://doi.org/10.1017/jfm.2018.741

Pegler, S. S. (2018b). Suppression of marine ice sheet instability. *Journal of Fluid Mechanics*, *857*, 648–680. https://doi.org/10.1017/jfm.2018.742

Pollard, D., DeConto, R. M., & Alley, R. B. (2015). Potential Antarctic Ice Sheet retreat driven by hydrofracturing and ice cliff failure. *Earth and Planetary Science Letters*, *412*, 112–121. https://doi.org/10.1016/j.epsl.2014.12.035

Rack, W., & Rott, H. (2004). Pattern of retreat and disintegration of the Larsen B ice shelf, Antarctic Peninsula. *Annals of Glaciology*, *39*, 505–510. https://doi.org/10.3189/172756404781814005

Renshaw, C. E., & Schulson, E. M. (2001). Universal behaviour in compressive failure of brittle materials [5]. *Nature*, *412*(6850), 897–900. https://doi.org/10.1038/35091045

Rignot, E., Casassa, G., Gogineni, P., Krabill, W., Rivera, A., & Thomas, R. (2004). Accelerated ice discharge from the Antarctic Peninsula following the collapse of Larsen B ice shelf. *Geophysical Research Letters*, *31*(18). https://doi.org/10.1029/2004GL020697

Robel, A.A., & Banwell, A. (2019). A speed limit on ice shelf collapse through hydrofracture.

Scambos, T. A., Bohlander, J. A., Shuman, C. A., & Skvarca, P. (2004). Glacier acceleration and thinning after ice shelf collapse in the Larsen B embayment, Antarctica. *Geophysical Research Letters*, *31*(18). https://doi.org/10.1029/2004GL020670

Schoof, C. (2007). Ice sheet grounding line dynamics: Steady states, stability, and hysteresis. *Journal of Geophysical Research: Earth Surface*, *112*(3). https://doi.org/10.1029/2006JF000664

Schulson, E. M. (2002). Compressive shear faults in ice: Plastic vs. Coulombic faults. *Acta Materialia*, *50*(13), 3415–3424. https://doi.org/10.1016/S1359-6454(02)00154-4

Schulson, Erland M., & Duval, P. (2009). *Creep and fracture of ice*. *Creep and Fracture of Ice* (Vol. 9780521806). https://doi.org/10.1017/CBO9780511581397

Schulson, Erland M., & Fortt, A. L. (2012). Friction of ice on ice. *Journal of Geophysical Research B: Solid Earth*, *117*(12). https://doi.org/10.1029/2012JB009219

Sergienko, O., & Macayeal, D. R. (2005). Surface melting on Larsen Ice Shelf, Antarctica. *Annals of Glaciology*. https://doi.org/10.3189/172756405781813474

Ultee, L., & Bassis, J. (2016). The future is Nye: An extension of the perfect plastic approximation to tidewater glaciers. *Journal of Glaciology*, *62*(236), 1143–1152. https://doi.org/10.1017/jog.2016.108

Figure 1: *Model framework. a) Failure regimes in ice as a function of the strain rate and confinement ratio of least- to most-compressive stress ($R=\sigma_3/\sigma_1$), adapted from Renshaw & Schulson (2001) and others cited in section 2.1. The mechanisms driving the three failure regimes are illustrated schematically along the top. Red lines show critical strain rates separating microscopic creep (shaded gray) from macroscopic plastic failure. The blue dashed line is the Tensile-Coulombic transition at R=0.01; the blue solid line is the Coulombic-Thermal Softening transition at R=1/3 for μ=0.5 (Schulson & Fortt, 2012). (b-c) Schematics illustrating model set-up and transition from b) the fully supported ice cliff to c) the full removal of the buttressing ice shelf. Ice is green and water is blue.*

Figure 2: *Depth-dependent (1-D) analytic model for stresses and strain rates along the face of an ice cliff after buttressing stresses are removed over a transition time Δt. We plot three cases: h=100 m, Δt=0.6 days (orange); h=600 m, Δt=0.6 days (cyan); h=100 m, $\Delta t=0.6\times10^{-4}$ (magenta). Sea-level (y=h) is plotted in gray. (a) The vertical overburden stress (σ_1) is plotted in black. For h=100 m, the horizontal hydrostatic stress (σ_3) is plotted in green. The effective deviatoric stresses ($\tau_e=(\sigma_1-\sigma_3)/2$) are plotted in orange/magenta/cyan. (b) The confinement ratios (σ_3/σ_1) are plotted in orange/magenta/cyan and pass through the deformation regimes delineated by the dark blue lines. (c) The effective strain rates are calculated from effective stresses, assuming a Maxwell viscoelastic rheology and prescribing some Δt (see legend). Strain rates above the tensile brittle-ductile transition are shaded red. d) Strain rates versus confinement ratio are overlain on the deformation-regime map.*

Figure 3: *2-D numerical simulations for three different ice cliffs (as in **Figure 2**), at the end of*

*their transitions (the penultimate time-step, $t/\Delta t=0.98$; see **Movie S1** for all time-steps). From left to right, cliffs have subaerial heights of 100, 100, and 600 m and associated transition times of 0.6, 6×10^{-4}, and 0.6 days. The total ice thickness is set such that the cliff is at flotation (note the 600-m case extends to 6 km and is truncated here) – the grounding line and cliff edge is at $x=0$. The top row shows effective strain rates within the cliff face. The color map is centered around the tensile brittle-ductile strain rate of 4×10^{-7} 1/s. The red lines show the location of the surface and base of the buttressing ice shelf. At this timestep, these lines nearly overlap as the shelf is thin. The middle row shows confinement ratios (R), color-coded by deformation regime: Thermal Softening (purple), Coulombic (gray), Tensile (green). The bottom row shows the difference between local and critical strain rates (defined separately for each deformation regime). Failure is predicted in the positive (red) zone.*

Figure 4: *Subaerial height (h) of a marine ice cliff versus the removal time of a buttressing ice-shelf (Δt). Analytically derived effective strain rates are colored in red/blue. Effective viscosities are calculated assuming the cliff is at flotation. We predict brittle failure (red) above the tensile brittle-ductile transition (solid green line) and ductile deformation (blue) at lower strain rates. Deformation is primarily viscous when the removal timescale is much longer than the relaxation time (black line), and elastic for shorter timescales. a) Comparison with previous studies. The hatched cyan region shows published values for the predicted onset of faulting in damaged ice near pre-existing cliffs (Bassis & Walker, 2012; Parizek et al., 2019; Ultee & Bassis, 2016). The yellow line shows the 90-m critical height prescribed by DeConto and Pollard (2016). b) Sensitivity to variations in the material properties of ice, specifically the grain size/fracture*

toughness (shaded green), flow-law parameter (dashed green lines), and effective viscosity prescribed by the total ice thickness (gray line).

Figure 1.

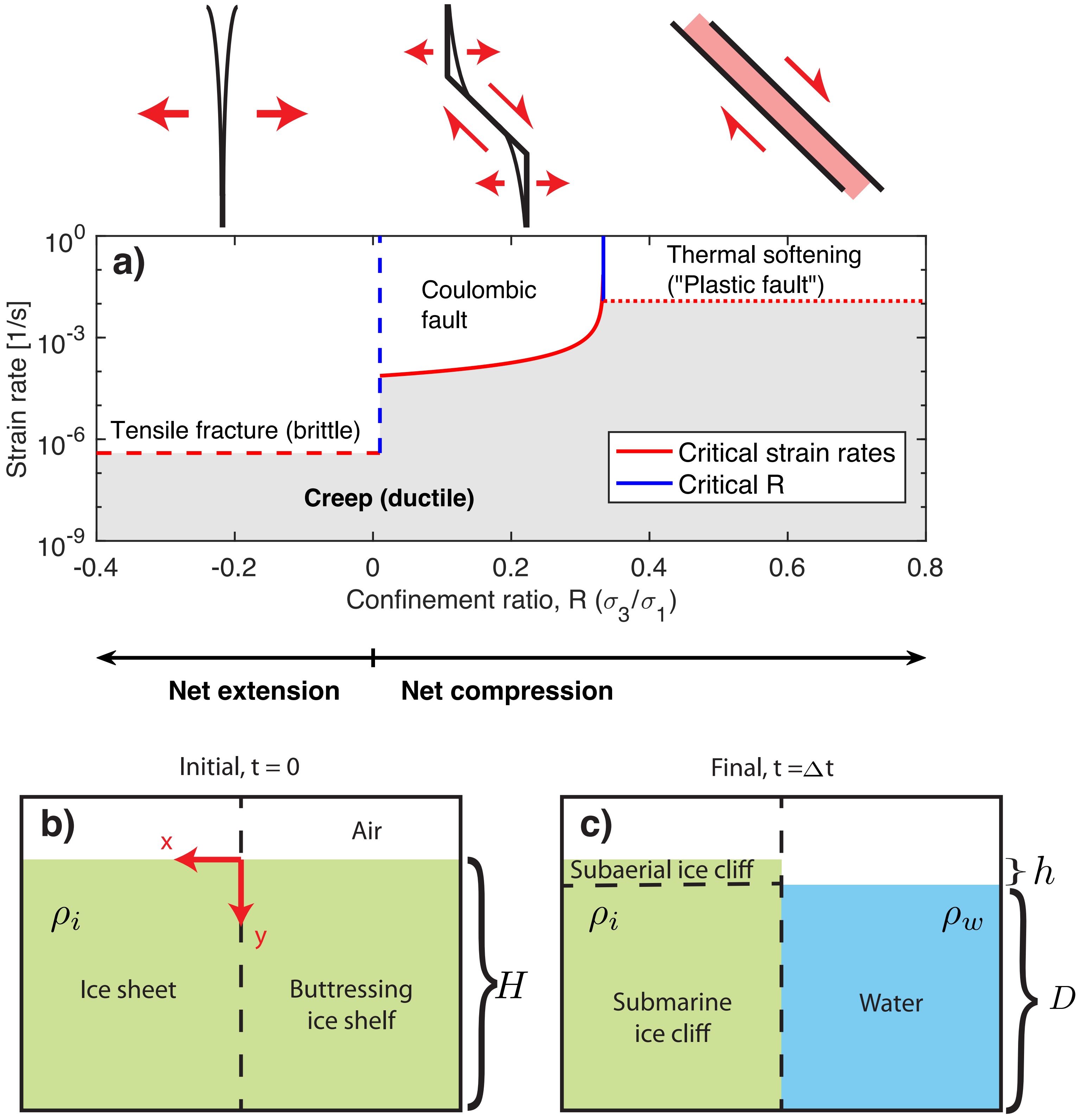

a)
Coulombic fault
Thermal softening ("Plastic fault")
Tensile fracture (brittle)
Creep (ductile)
Critical strain rates
Critical R
Strain rate [1/s]
Confinement ratio, R (σ_3/σ_1)
Net extension
Net compression
Initial, t = 0
Final, t = Δt
b)
Air
x
y
ρ_i
Ice sheet
Buttressing ice shelf
H
c)
Subaerial ice cliff
h
ρ_i
ρ_w
Submarine ice cliff
Water
D

Figure 2.

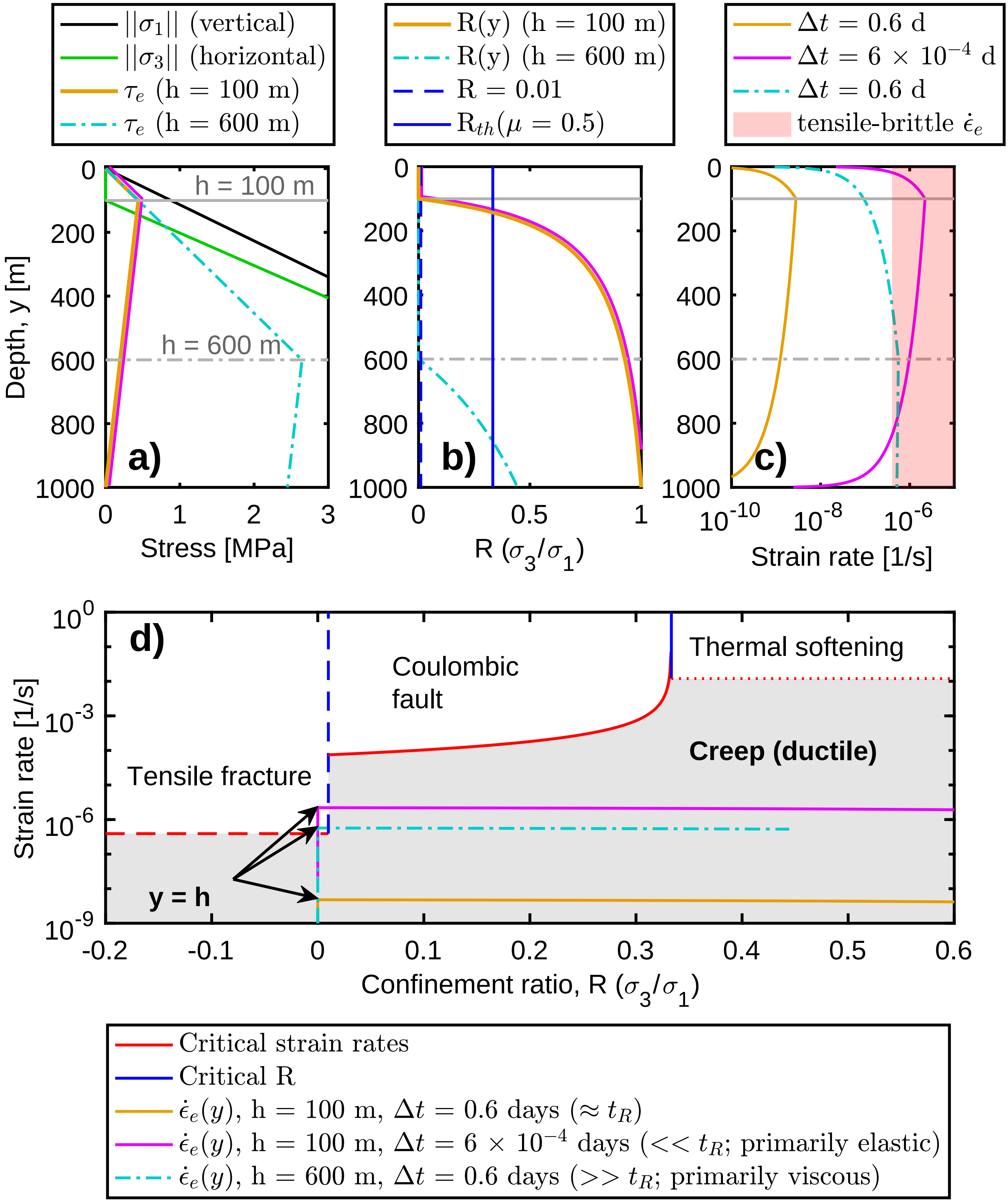

$||\sigma_1||$ (vertical)
$||\sigma_3||$ (horizontal)
τ_e (h = 100 m)
τ_e (h = 600 m)
R(y) (h = 100 m)
R(y) (h = 600 m)
R = 0.01
$R_{th}(\mu = 0.5)$
$\Delta t = 0.6$ d
$\Delta t = 6 \times 10^{-4}$ d
$\Delta t = 0.6$ d
tensile-brittle $\dot{\epsilon}_e$
h = 100 m
h = 600 m
a)
b)
c)
Depth, y [m]
Stress [MPa]
R (σ_3/σ_1)
Strain rate [1/s]
d)
Coulombic fault
Thermal softening
Creep (ductile)
Tensile fracture
y = h
Strain rate [1/s]
Confinement ratio, R (σ_3/σ_1)
Critical strain rates
Critical R
$\dot{\epsilon}_e(y)$, h = 100 m, $\Delta t = 0.6$ days ($\approx t_R$)
$\dot{\epsilon}_e(y)$, h = 100 m, $\Delta t = 6 \times 10^{-4}$ days ($<< t_R$; primarily elastic)
$\dot{\epsilon}_e(y)$, h = 600 m, $\Delta t = 0.6$ days ($>> t_R$; primarily viscous)

Figure 3.

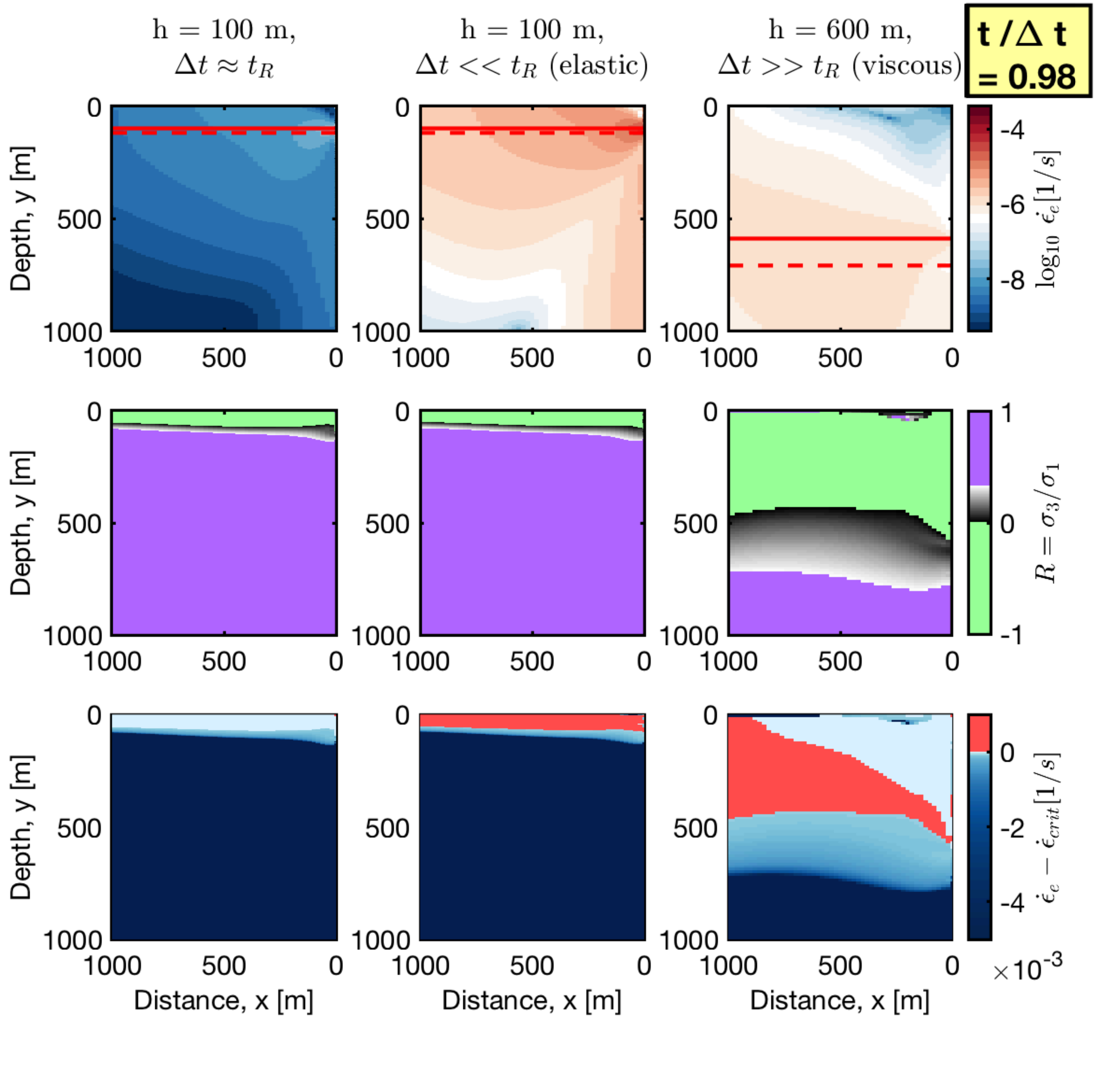

h = 100 m,
$\Delta t \approx t_R$
h = 100 m,
$\Delta t << t_R$ (elastic)
h = 600 m,
$\Delta t >> t_R$ (viscous)
t / Δ t
= 0.98
Depth, y [m]
Distance, x [m]
$\log_{10} \dot{\epsilon}_e [1/s]$
$R = \sigma_3/\sigma_1$
$\dot{\epsilon}_e - \dot{\epsilon}_{crit} [1/s]$
$\times 10^{-3}$

Figure 4.

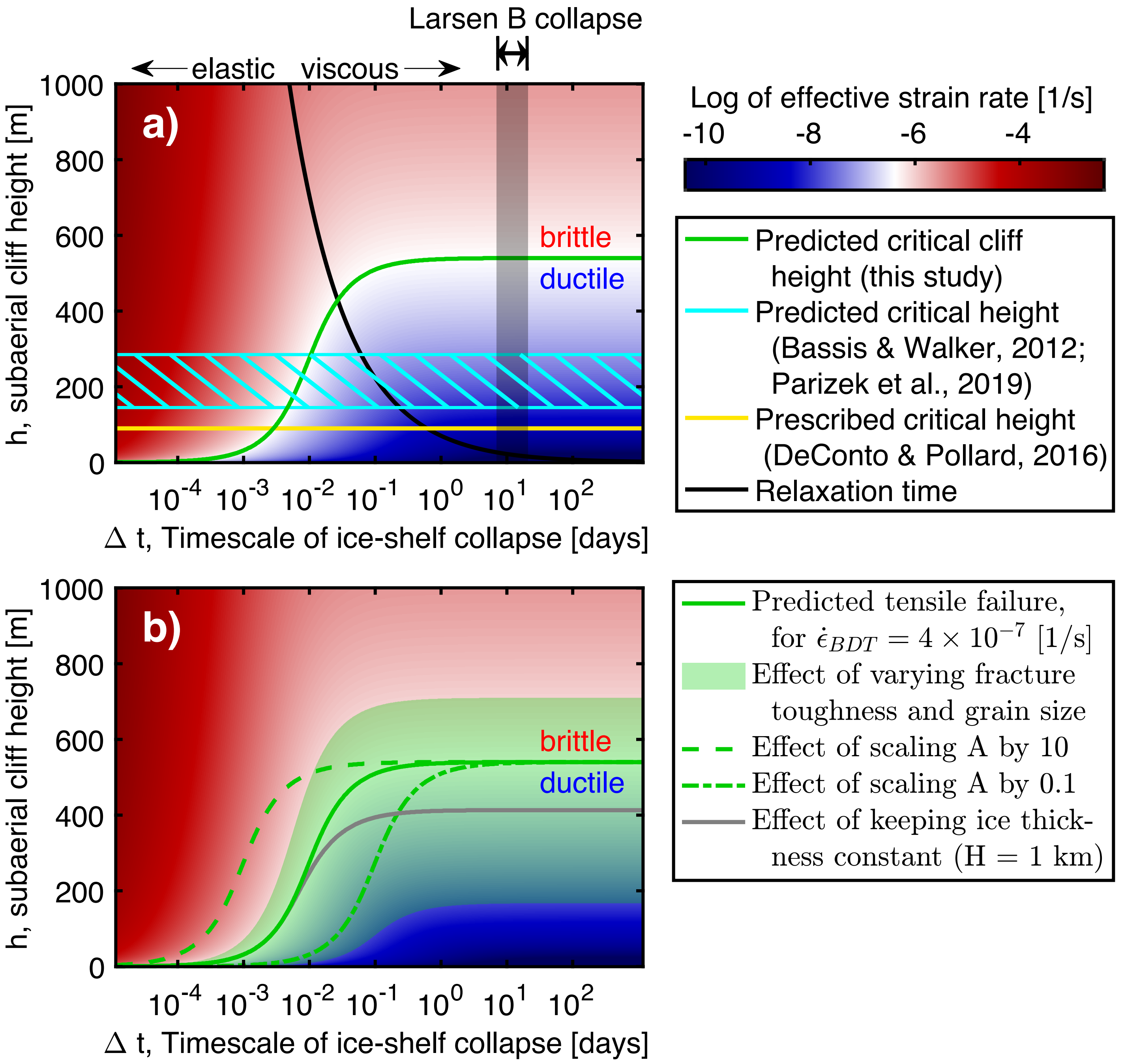

Larsen B collapse
elastic
viscous
a)
brittle
ductile
h, subaerial cliff height [m]
1000
800
600
400
200
0
10^{-4} 10^{-3} 10^{-2} 10^{-1} 10^{0} 10^{1} 10^{2}
Δ t, Timescale of ice-shelf collapse [days]
Log of effective strain rate [1/s]
-10 -8 -6 -4
Predicted critical cliff height (this study)
Predicted critical height (Bassis & Walker, 2012; Parizek et al., 2019)
Prescribed critical height (DeConto & Pollard, 2016)
Relaxation time
b)
brittle
ductile
Predicted tensile failure, for $\dot{\epsilon}_{BDT} = 4 \times 10^{-7}$ [1/s]
Effect of varying fracture toughness and grain size
Effect of scaling A by 10
Effect of scaling A by 0.1
Effect of keeping ice thickness constant (H = 1 km)